Investigating radiation-induced segregation on intragranular defects in a 316L(N)

Solène Rouland, Bertrand Radiguet, Philippe Pareige

Investigating radiation-induced segregation on intragranular defects in a 316L(N)

Solène Rouland, Bertrand Radiguet, Philippe Pareige

Université de Rouen Normandie, CNRS, INSA Rouen, Groupe de Physique des Matériaux, 76000 Rouen, France.

Corresponding author : solene.rouland@univ-rouen.fr

Abstract

Radiation induced segregation (RIS) on lattice defects and phase stability under irradiation have been investigated in an optimized solution annealed 316L(N) with an increased content of N and a significant amount of Nb. Primary Z-phase nitrides were observed within the as-received microstructure. 5 MeV Fe^{3+} ion irradiation was conducted at 450°C up to 1dpa. Post-ion irradiation characterization was performed via nanoscale techniques coupling and correlation to associate radiation induced defects such as cavities and dislocation loops to the local chemistry. Cr, Fe and Ni observed RIS trends were expected, but P was solely measured at the vicinity of cavities. Void-precipitate association has been detected thanks to transmission electron microscopy (TEM) and it is believed to explain the low reduced atomic density measured at the location of a feature within an atom probe tomography (APT) volume. Nb-rich novel features were observed after irradiation and first results are brought to establish a link between these features and the primary Z-phase.

Key words: radiation-induced segregation, austenitic stainless steels, TEM-APT correlative microscopy, ion irradiation, Z-phase.

1. Introduction

Austenitic stainless steels are employed as structural materials in current commercial reactors, they are candidates for advanced nuclear systems and are considered for fusion reactors [1].

Radiation-induced segregation (RIS) has been proven to be one of the various synergetic parameters which are involved in irradiation-assisted stress corrosion cracking (IASCC) [2] and void swelling [3] degradation mechanisms. They can respectively lead to an unexpected failure and unacceptable dimensional changes of affected components. Therefore, to understand and describe mechanisms involved in RIS is of prime importance for nuclear materials science.

On one hand, RIS is mainly studied at grain boundaries because IASCC provokes an intergranular fracture. Irradiation hardening is conjointly involved with RIS [4]. This increase in yield strength is due to the multiplication of obstacles generated during irradiation impeding dislocation motion, e.g. lattice

defects. Lattice defects nature, number density, size, sink strength, bias, and RIS levels and tendencies at their vicinity, influence both hardening and segregation at grain boundaries. In addition to chemical redistribution under irradiation, RIS can lead to phase instabilities and sometimes precipitate-defect association [5].

On the other hand, void growth rate is thought to be influenced by kinetics of vacancy-mediated diffusing species involved in RIS [6].

Many authors observed RIS on different types of sinks, i.e. grain boundaries [4, 7–11], dislocation loops [10–14] and lines [11, 15] and cavities [8, 13, 14]. (S)TEM and APT are extensively used to study microstructural features induced by radiation damage because of their complementarity: accurate crystallography information for TEM and accurate composition measurements for APT. Combining STEM imaging with X-ray Energy Dispersive Spectroscopy (EDS) mapping permits to clearly reveal RIS on characterized crystal defects. However, EDS is not able to provide quantitative enrichments because of the contribution to the signal of the surrounding matrix, the 2D projection through specimen depth and the absorption of light elements. Access to crystallographic information thanks to APT is limited.

Correlative TEM-APT studies have illustrated the direct comparison of same features by both techniques, which can offer both compositional and crystallographic information [16]. Correlative microscopy has been recently used as a new tool to study radiation damage [12, 17–19].

The aim of this paper is to investigate RIS and phase stability on different types of lattice defects in an optimized 316L(N) to identify mechanisms involved. TEM-APT coupling or correlative approach has been applied to study RIS in an ion irradiated 316L(N) austenitic stainless steel.

2. Experimental

2.1. Material and heavy ion irradiation

A block of 316L(N), i.e. an optimized 316L with an increased content in N, was supplied by EDF R&D. The nominal composition of the studied steel given in Table 1 has been obtained thanks to the infrared absorption method after combustion for C and S, by the inert gas fusion technique for N and by X-ray Fluorescence Spectroscopy for the other alloying elements. The composition is in line with RCC-MRx-2018 specifications [20] except for its increased nitrogen content up to 0.1 wt.%. Nitrogen was added to improve mechanical properties (tensile, creep) and also because it is a strong austenite stabilizer [21], [22]. The sheet, from which the block was extracted, was hot rolled by cross rolling passes to a thickness of 40 mm. Then, the steel was solution annealed at 1085°C during 1h followed by a water quenching. Nb and Ti contents are not specified for the 316L(N) grade by the code, but these minor elements are playing a role in the solution-annealed microstructure. If Nb and Ti additions are sufficient with respect to the C and N content, they can stabilize steels by promoting the formation of fine intergranular

carbides, nitrides or carbonitrides of MX type with (M=Nb, Ti and X=C,N) [23], [24]. Austenitic stainless steels stabilized grades Type 321 contains a minimum of 5 × [C] Ti whereas type 347 a minimum of 10 × [C] Nb. Regarding the nominal chemical composition, the studied steel is not stabilized by Nb, but the role of Ti cannot be determined.

Table 1. Nominal composition (Nom.) of the studied 316(N) steel versus RCC-MRx specifications (Spec.) in wt.% - Fe in balance . p.c. = content relative to the purity class. n.s. = not specified, impurity. n.m. = not measured.

	B	C	Co	Cr	Cu	Mn	Mo	N	Nb	Ni	P	Si	S	Ti
Spec.	≤ 20 ppm	≤ 0.03	p.c.	17.0-18.0	≤ 1.00	1.60-2.00	2.30-2.70	0.06-0.08	n.s.	12.0-12.5	≤ 0.030	≤ 0.50	≤ 0.015	n.s.
Nom.	19 ppm	0.021	0.03	17.7	0.06	1.71	2.46	0.1	0.09	12.6	0.021	0.42	0.002	n.m.

Specimens studied were sampled from the half-thickness of the sheet. Prior irradiation, solution-annealed specimens were cut in 3 mm diameter disks and mechanically ground and polished down to a thickness of ~ 300 µm. Colloidal silica was used for the last polishing step. Irradiation was performed in the implantation beam line connected to the 2 MV Tandem/Van de Graff ARAMIS (Accelerator for Research in Astrophysics, Microanalysis and Implantation in Solids) accelerator [25] of the JANNuS-SCALP (Synthesis and Characterization using ion AcceLerators for Pluridisciplinary research) platform [26], located in the CSNSM laboratory, Orsay. Irradiation was conducted under a vacuum level below 5 x 10^{-6}mbar with Fe^{3+} ions having an energy of 5 MeV. The ion beam was focused and raster-scanned. Based on SRIM simulations, the Bragg peak depth from the sample surface would be at ~ 1.5µm. 1 displacement per atom (dpa) in average at a damage rate of 4.2 x 10^{-5} dpa.s^{-1} was reached in the region of interest, from 100 nm to 500 nm depth below the surface (Fig. 1). Calculations were made according to Stoller recommendations [27]: Kinchin–Pease model with the selected option 'Ion Distribution and Quick Calculation of Damage'. The irradiation temperature is estimated to be equal to 450 ± 20°C (see Appendix A).

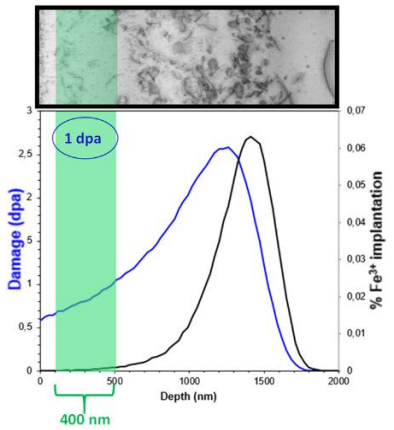

Fig. 1. (Color online) Damage and implantation profiles along specimen depth and specimen cross-section imaged with STEM bright-field (BF) at 0° **B**~$[01\bar{1}]$ showing the total depth of the irradiated zone (~2 µm). The green area corresponds to the 1 dpa region of interest, defined between 100 and 500 nm depth below the surface.

2.2. Pre- and post-irradiation characterization

Nanoscale characterisation was carried out with Transmission Electron Microscopy (TEM) and Atom Probe Tomography (APT). Specimens were prepared thanks to the Dual-Beam Zeiss XB-540 equipped with electron backscattered diffraction (EBSD) using a Ga^+ Focused Ion Beam (FIB) source at 30kV.

To check elemental distribution within the matrix prior to irradiation, lifted out chunks were mounted onto individual posts of a Si microtip coupon then annular milled for APT tips preparation, final cleaning was performed using a 2kV ion beam.

For coupled S/TEM imaging with STEM-EDS mapping at the solution-annealed and the irradiated states, TEM lamellae were mounted onto Cu or Mo TEM half-grids, then thinned down to 120 nm. Lamellae were back-polished under a low-voltage Ar^+ ion beam (0.5 keV) until the desired thickness was reached in the Precision Ion Polishing System II (PIPS II) from Gatan [28].

For TEM-APT correlative microscopy on irradiated specimen, APT tip orientation was selected with EBSD. As Frank loops are one of the most observed defect type for the chosen irradiation conditions, the selected cross-section tip orientation was selected close to zone axis <011>. Near this zone axis most defects exhibit residual contrast in S/TEM BF images, even at 0° tilt. Furthermore, the tilt angles needed to reach the diffraction conditions of interest are lowered reducing the dimensional bias of the tilted projected tip. APT tips were mounted on W TEM grids with pretips (i.e. pillars). The correlative microscopy holder was fabricated based on the plans shared by M. Herbig [16]. This holder allowed an easy-transfer of tips between three instruments: FIB for tip preparation, TEM for defect crystallography characterization and APT for measurement of chemical heterogeneities at the atomic scale.

TEM and STEM-EDS characterizations were carried out using a JEOL-ARM200F (cold-FEG, HR pole piece) aberration-corrected both in probe (STEM mode) and in image-forming optics (TEM mode) and operated at 200 kV. This electron microscope is equipped with a Gatan Imaging Filter Quantum ER and a single JEOL Centurio EDS silicon drift detector (SDD) having a collection solid angle of 0.98 steradians from a detection area of 100 mm^2. To quantify the defect number density, the average thickness of each TEM lamella was measured by electron energy loss spectroscopy (EELS) in energy-filtered TEM (EFTEM) mode. All measured TEM lamella thicknesses are in the range of 60-100 nm with a typical error of 15-20% [29]. A double-tilt analytical specimen holder was used to reduce shadowing effect during STEM-EDS acquisitions. Specimens were tilted to reach targeted diffraction conditions for imaging and diffraction whereas EDS data were acquired at zero tilt angle to maximise the signal on the SDD. EDS spectrum images have been collected and processed with JEOL Analysis Station commercial software. A compromise between a sufficient spatial resolution and high statistics were found to define the acquisition parameters: dead time of 20%, condenser aperture size of 50 µm, 0.2 nm spot size (JEOL notation 4C), scanned area = 256x256 px^2, dwell time = 0.5 msec, total acquisition time > 2h. The STEM-EDS spectrum image dataset post-treatment consisted in: binning =

3x3, background subtraction, automatic peak deconvolution following peak identification. The k-factor quantification method was used but no absorption correction was applied resulting in semi-quantitative measurements of composition.

APT tips were analysed in a Cameca LEAP 4000X HR. Prior irradiation, APT experiments were conducted in voltage mode, at 63K, a pulse frequency of 200kHz, and a pulse ratio of 20%. The detection rate was raised during the analyses from 0.0005 to 0.0015 ion/pulse to work under a constant evaporation flux of 0.15 ion/s/nm^2. Post-irradiation APT experiments for correlative microscopy purpose were performed in laser mode at relatively high temperature (80K) to diminish risk of tip fracture. The pulse energy was calculated for an effective pulse fraction of 20% and ranged from 15 to 25 pJ. The pulse frequency was equal to 250kHz. If the specimen did not fracture during the analysis, the tip was imaged again by TEM to estimate the evaporated length and ensure a reliable 3D reconstruction. The collected data were processed with the Cameca IVAS commercial software and the GPM 3D soft software.

The dislocation density in the solution-annealed 316L(N) was measured by the line intercept and the line-length measurement methods on STEM images thanks to the ImageJ software on two different lamellae oriented downzone at two different zone axes. To correct the total dislocation line length from the measured total projected length l_p, l_p was multiplied by $\frac{4}{\pi}$ [30].

The 1 dpa damaged zone was imaged under various techniques and diffraction conditions. The two edge-on variants of Frank loops at B=[01$\underline{1}$] were observed with the use of the relrod dark-field (RRDF) technique and dislocation analysis (i.e. invisibility criterion) was performed to distinguish between the two other Frank loop variants and perfect loops.

Frank loops quantification was only based on RRDF micrographs. Their number density was obtained by multiplying by four the total number of measured Frank loops per volume for one family. Calculation was done for both families, then averaged. A total number of 99 Frank loops were characterized over an area of 5.3 µm^2, this number includes the two imaged variants. The size measurements of the loops were performed thanks to the ImageJ software.

Cavities were revealed thanks to out-of-focus TEM imaging ($\pm$ 2 µm). They appear as white dots surrounded by a dark fringe in underfocused images, and as dark dots surrounded by a bright fringe in overfocused images. The specimen was tilted away from a low index zone axis in order to limit diffraction contrast from the other features present in the region of interest. Cavities size measurements were performed manually. A total number of 986 cavities were characterized over an area of 1.4 µm^2 and 14 over an area of 2.2 µm^2 for small and large cavity populations respectively on various TEM lamellae. The cavity number density was determined for each population as well.

The errors [31] in the determination of the density ε_{N_d} was calculated this way:

$$\varepsilon_{N_d} = \underline{N_d}\sqrt{\left(\frac{\sqrt{N}}{N}\right)^2 + \left(\frac{\varepsilon_t}{t}\right)^2} \quad (1)$$

and average size errors ε_d was determined thanks to this formula:

$$\varepsilon_d = \sqrt{\left(\frac{s.d.}{\sqrt{N}}\right)^2 + {\varepsilon_m}^2} \quad (2)$$

Where ε_t is the error of thickness measurement taken as 20% of the measured thickness t, s.d. is the standard deviation in size, ${\varepsilon_m}^2$ is the measurement error taken as the size of a pixel in the image, $\underline{N_d}$ is the mean number density and N is the total number of cavities or Frank loops.

Linear profiles extracted from EDS spectrum images were smoothed by applying a moving average while error bars have been defined by a moving standard deviation. Contribution of the Mo grid to the signal was roughly estimated by the difference in measured Mo concentration within the matrix between the same material welded on a Cu grid (as-received state) and Mo grid (ion irradiated state). All lamellae were oriented in a similar way toward the EDS detector. Mo contribution from the grid was subtracted and concentrations were then normalized.

APT 3D volumes were reconstructed thanks to correlative microscopy. At the as-received state, SEM images were used. After irradiation, the reconstruction parameter k, was adjusted based on the depth between the tip apex and the feature #2 measured on the corresponding TEM image of the tip. The microfracture depth was determined by translating the as reconstructed volume along the tip axis z to reach the total evaporated depth determined from TEM images taken before and after performing APT analysis. The feature #4 observed in the APT volume was then correlated to the contrasts observed on the TEM image of the tip. The standard value of ξ of 1.6 was used for the reconstruction. The composition measurements were performed from the mass spectrums extracted from : a sub-volume for the matrix, isolated atoms from isoconcentration surfaces for the features #1 and #2. A linear profile was drawn across the feature #4. Peak decomposition was done on overlapped peaks and the calculated isotope abundances were compared to the natural ones. As recommended [32], APT standard deviation s.d. of composition measurements was determined thanks to this equation:

$$s.d. = \sqrt{[X](1-[X]) \times \frac{1-Q}{N}} \quad (3)$$

Where [X] is the atomic concentration of the element X, Q is the detection efficiency (equal to 36% for the LEAP 4000X HR) and N the total number of detected atoms within the analysed volume. In order to identify significant enrichment or depletion of chemical elements at features location compared to the matrix, the relative error, defined as the ratio between the standard deviation and the measured composition, was calculated and compared to an enrichment factor, defined as the ratio between the

feature and the matrix composition. If the absolute value of the difference between the enrichment factor and 1 is lower than the relative error, then the change in composition is not significant to conclude any enrichment or depletion. An enrichment factor higher than 1 stands for an enrichment, while element deplete if this factor is lower than 1.

3. Results

3.1. As-received material characterization

At the microscale, the equiaxed grain diameter is about 50 µm and does not exhibit crystallographic texture. Warm rolling produces ribbons of residual δ-ferrite (less than 0.01 surface fraction) and microsegregations parallel to the rolling direction. These chemical heterogeneities are enriched in ferrite stabilizer elements and Mn. Majority of micron-size particles are aluminium oxides inclusions. These inclusions are typical for 316L grades [33]. Nb-rich precipitates were also found at this scale. These results obtained with SEM-EBSD and EDS are presented in the Supplementary Material document (Appendix B).

Within the matrix, APT experiments show that elements are homogeneously distributed (Fig. 2a). The dislocation density measured by TEM (Fig. 2b) is higher than for solution annealed 316/L grades: 10^{14} m^{-2} vs. 10^{10} [34] to 10^{13} m^{-2} [35] but the measured magnitude is the same as in a nitrogen stabilized 316LN [36].

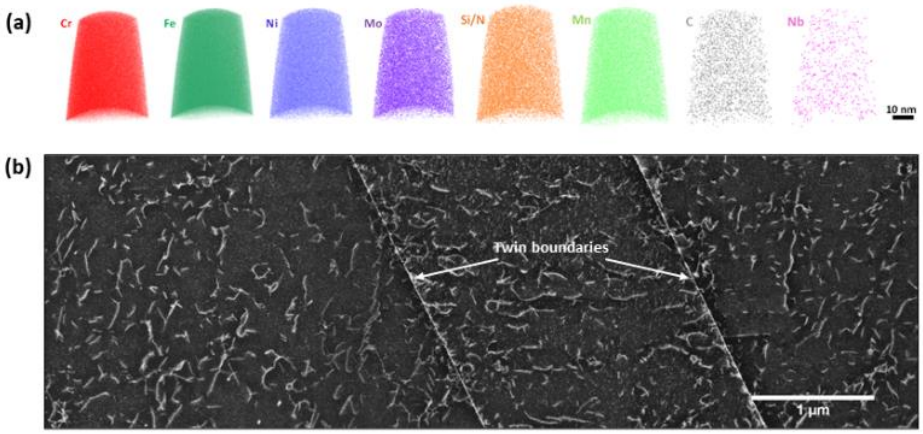

Fig. 2. (Color online) (a) Homogeneous distribution of elements within an APT 3D-volume. (b) STEM low-angle annular dark-field (LAADF) image oriented downzone with **B**=<110> that served to calculate the as-received dislocation density.

At the nanoscale, the presence of nano-sized precipitates was detected thanks to Z-contrast imaging in STEM high-angle annular dark-field (HAADF) mode (Fig. 3a). The precipitates are enriched in N, Cr, Nb and Mo (Fig. 3b and 3c) with a number density of 4.5 x 10^{18} m^{-3}. Local enrichments in Ti are sometimes observed within the precipitates (Fig. 3b and 3d).

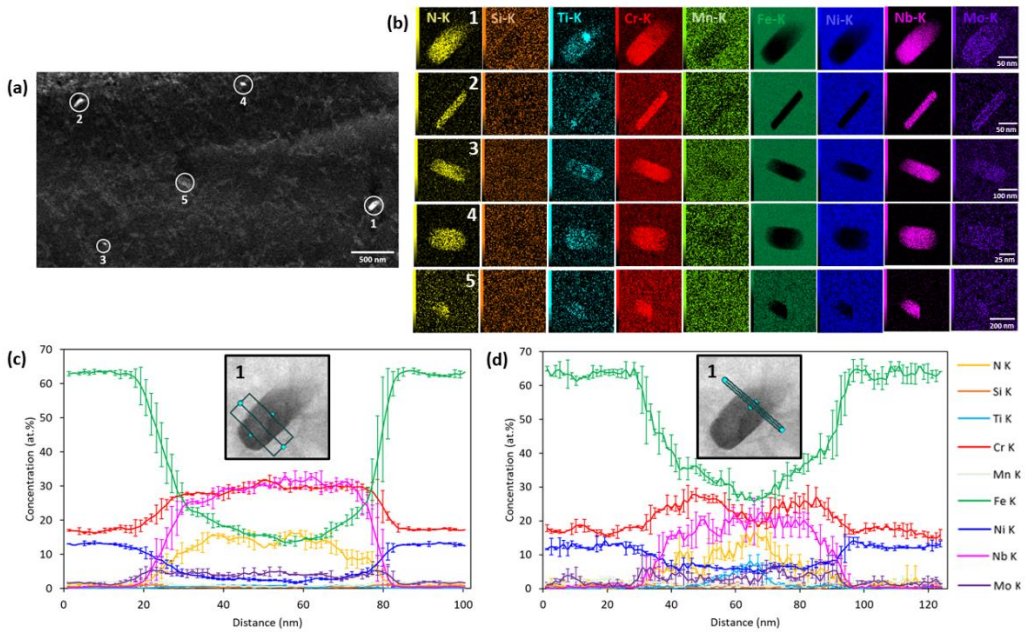

Fig. 3. (Color online) (a) STEM HAADF image revealing the presence of high Z precipitates in bright. (b) STEM-EDS elemental maps of the precipitates circled in (a). (c) and (d) EDS line profiles drawn across the precipitate #1 and the corresponding STEM BF image in the as-received material.

Contrasts observed in the STEM bright field (BF) image in Fig. 3c and 3d indicate that the precipitate #1 is tilted within the lamella depth and the upper part has been partly thinned by the FIB polishing. Thus, matrix contribution to the EDS signal is larger in the upper part of the precipitate. It is confirmed by comparing the concentrations measured across the precipitate in Fig. 3c and 3d: Nb, N and, to a lesser extent Cr, Mo (i.e. major alloying elements) concentrations are higher in thicker parts of the precipitates. Thus, Nb, N, Cr and Mo measured concentrations are underestimated. This underestimation is even more pronounced for N, a light element which is affected by a substantial X-ray absorption. These Nb-rich precipitates observed at the nanoscale show similar enrichments as the ones observed at the microscale. This suggests that they belong to the same family. These precipitates are thought to be Z-phase (CrNbN) [24]. Primary Z-phase, about 100 nm in size, has already been detected in a 316LN+Nb after solution annealing at 1050°C [37].

Contrary to Cr, Nb and N do not deplete at the Ti-rich location (Fig. 3d). In a 25Cr-20Ni-Nb-N austenitic stainless steel aged at 700°C, secondary NbN nitrides act as sites for the nucleation of secondary Z-phase [38]. MX and Z-phase can coexist at the solution-annealed state [24], [39], and complex carbonitrides (Nb,Ti)(C,N) of MX type can be present in steels containing sufficient amount of Nb, Ti, C and N [24]. Z-phase could have nucleated from a MX precipitate during solution annealing. From authors' literature review, Z-phase stability under irradiation has not been studied yet.

3.2. Microstructure evolution under irradiation

Cavities and Frank loops populations study is carried out within the 1 dpa region of interest. To identify cavities, lamella was first titled away from the zone axis. Then, out-of-focus imaging was performed for

identification and counting (Fig. 4). Two populations of cavities, distinguished by their size and number densities, coexist. Small cavities are heterogeneously distributed and some of them are aligned along dislocation lines (Fig. 4d and 4e). The population of small cavities has appropriately three times smaller average size than the population of large cavities and their number density differs by two orders of magnitude (Table 2).

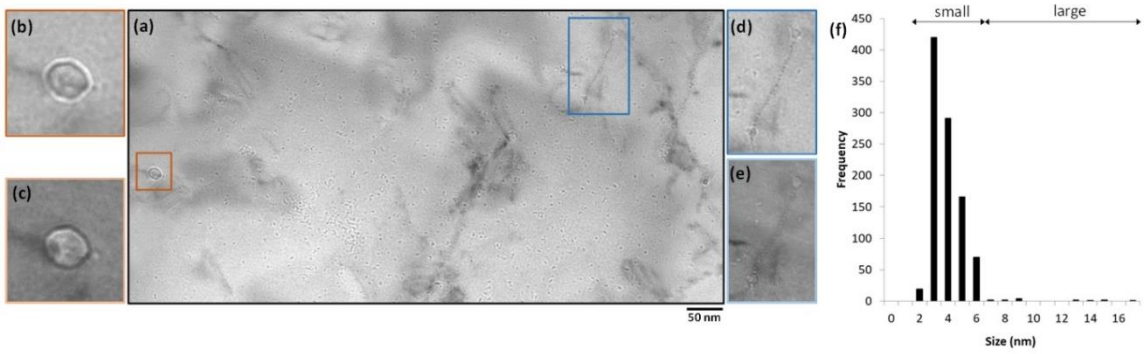

Fig. 4. (Color online) (a) TEM BF overfocused image showing cavities bimodal distribution in size. The orange square highlights a large cavity in (b) overfocused and (c) underfocused images. The blue square indicates small cavities located along a dislocation line in (d) overfocused and (e) underfocused images. (f) Size distribution histogram.

Thanks to the RRDF technique, two families of Frank loops over the four existing ones were imaged (Fig. 5). The standard deviation is large. Indeed, their size ranges from 8 to 136 nm (Table 2).

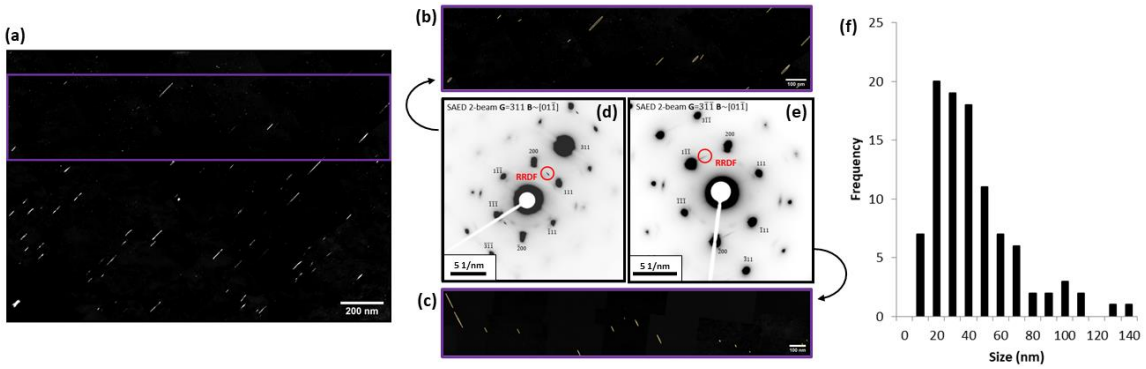

Fig. 5. (Color online) Frank loops lying on (a) and (b) ($\underline{1}11$) and (c) ($\underline{111}$) planes imaged thanks to the RRDF imaging technique, (d) and (e) corresponding diffraction conditions. Measurement was done within the 1 dpa damaged zone for the two variants (purple rectangle). (f) Size distribution histogram.

Results of the size measurement and number density are summed up in Table 2.

Table 2. Cavities and Frank loops size d and number density N_d.

	Cavities		Frank loops
	Small	Large	
Mean size $\underline{d} \pm \varepsilon_d$ (s.d.) in nm	3.4 ± 0.3 (0.9)	10.3 ± 1.0 (3.4)	38 ± 3 (27)
Min. / max sizes d_{min} / d_{max} in nm	1.3 / 6.0	6.1 / 16.1	8 / 136
Mean number density $\underline{N_d} \pm \varepsilon_{N_d}$ in m^{-3}	$9.4 \pm 1.9\ 10^{21}$	$8.0 \pm 2.7\ 10^{19}$	$8.5 \pm 1.9\ 10^{20}$

1.1. Radiation induced segregation on intragranular defects

Coupling of S/TEM imaging with STEM-EDS mapping permits a direct comparison of the measured chemical heterogeneities at the vicinity of pre-identified crystal defects. Fig. 6a, 6b, 7a and 7b show cavities and Frank loops within the 1 dpa damaged region in STEM BF and the elemental maps of two different areas.

From EDS elemental maps (Fig. 6b and 7b), Ni and Si enrichments are observed on all defect types. P enrichment is only observed at the cavity location, on all the cavities of the two analysed regions. Indeed, near cavities, the apparent specimen thickness is reduced, lowering the matrix contribution to the detected signal. Hence, P signal at dislocation location could be drowned in the background noise. Cr depletion is observed nearby all crystal defects. Fe exhibits a particular behaviour. Fe depletes at cavities and Frank loops location and is enriched at their vicinity, resulting in a 'M-shaped' concentration profile. Mn depletes on all defect types. Tendencies for Ti, N and Mo could not have been clearly established; their noisy profiles are not drawn for clarity.

All elements involved in RIS, namely Fe, Ni, Cr, Si, Mn and P, exhibit similar trends for all the defects. Nb enriches at the cavity location in the second analysed area (Fig. 7c) whereas no enrichment is observed on the cavity in the first analysed area (Fig. 6c). Nb has not been reported to enrich/deplete on radiation-induced extended defects location in austenitic stainless steels. Thus, this enrichment is likely to be due to the presence of an embryo or a nanoprecipitate at the cavity vicinity.

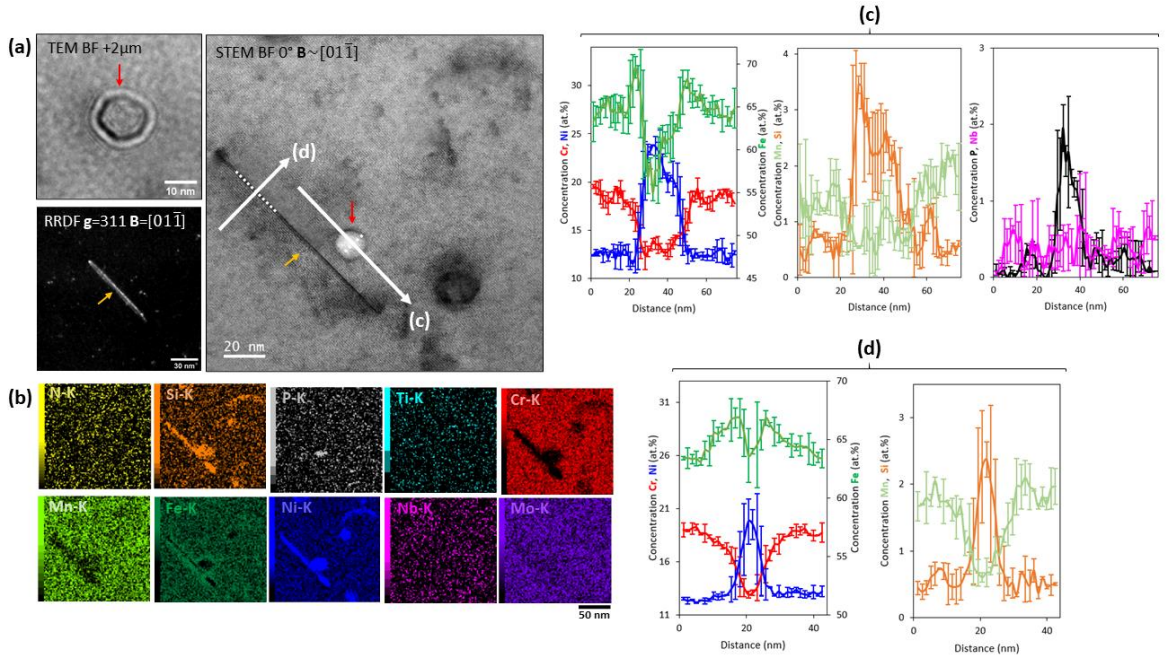

Fig. 6. (Color online) (a) First selected region for STEM-EDS analysis and the corresponding elemental maps (b). (a) also shows the defect nature determination thanks to various imaging techniques. The red and yellow arrows indicate the cavity and Frank loop viewed edge-on respectively. Concentration profiles extracted from two different locations of the STEM-EDS map passing through (c) a cavity and (d) a Frank loop. The white dashed lines in (a) represent the width of the line profile.

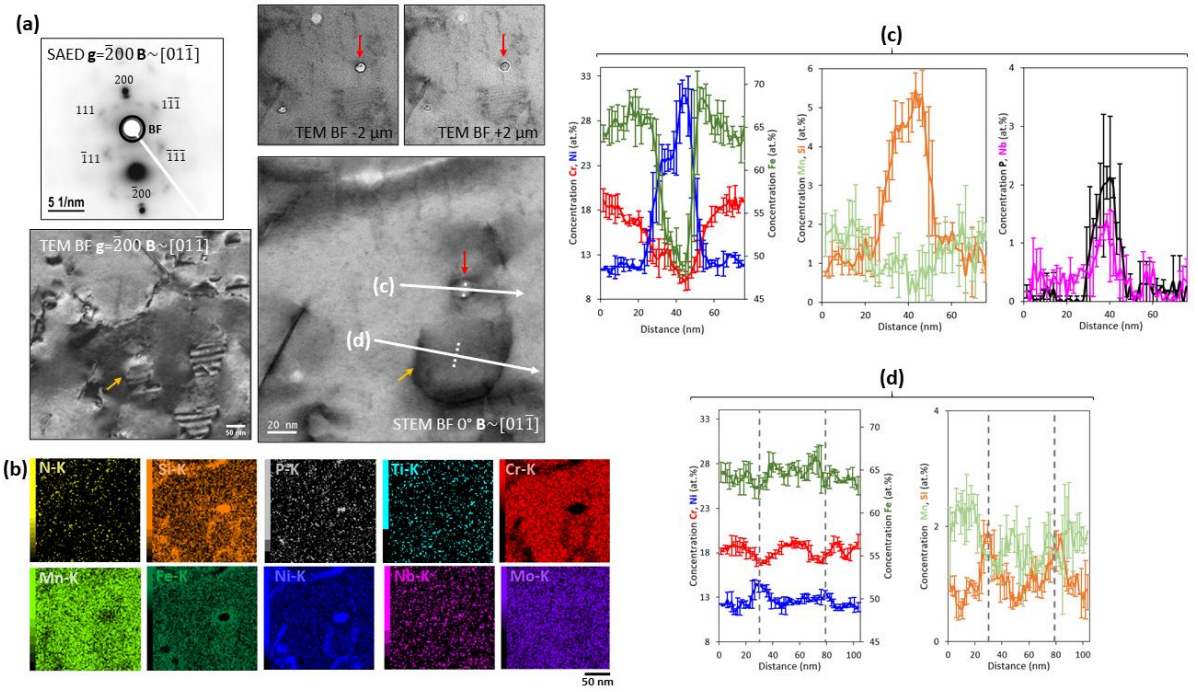

Fig. 7. (Color online) (a) Second selected region for STEM-EDS analysis and the corresponding elemental maps (b). (a) also shows the defect nature determination thanks to various imaging techniques. The red and yellow arrows indicate the cavity and the Frank loop respectively. Concentration profiles extracted from two different locations of the STEM-EDS map passing through (c) a cavity and (d) a Frank loop. The white dashed lines in (a) represent the width of the line profile and the grey dashed line in (d) indicate the border of the dislocation loop.

Correlative APT-TEM microscopy appears to be the suitable technique to overcome encountered quantitative chemical measurements issues, i.e. absorption of light elements, matrix contribution to the signal and defect superimposition within the depth of the lamella. As shown in Fig. 8a, the tip has been characterized before and after APT analysis. It allows to accurately measure the evaporated length for APT reconstruction and, typically, a reliable defect size measurement.

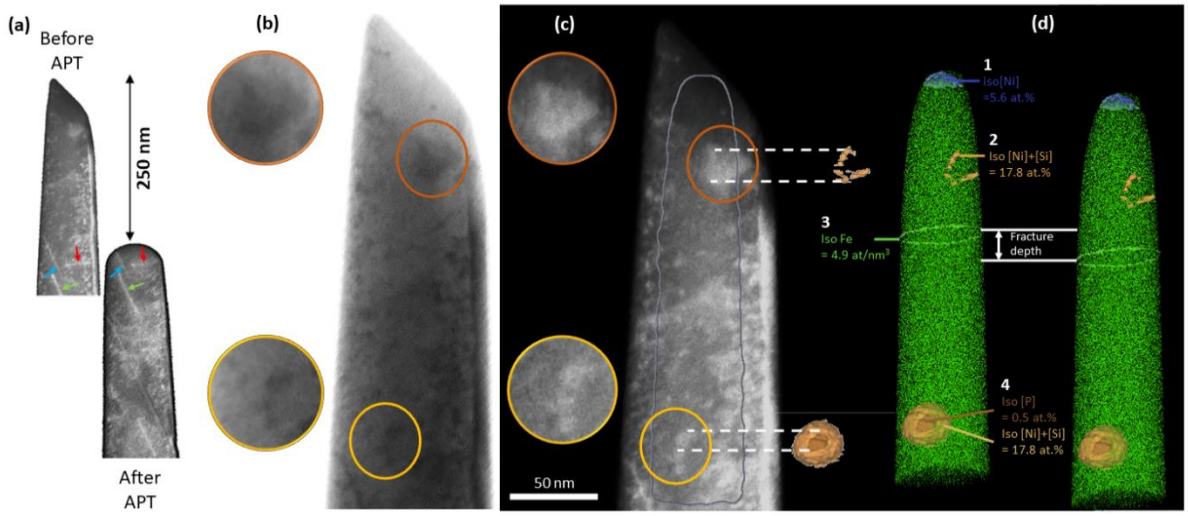

Fig. 8. (Color online) (a) STEM LAADF image of the tip before and after APT analysis taken at **B**=<011>. Correlation attempts between (d) the reconstructed APT volume and the tip imaged in (b) STEM BF and (c) STEM LAADF at **B**=<011>. 4 features are observed within the APT volume.

Over the four features observed within the APT tip volume (Fig. 8d), two of them, features #2 and #4, could be correlated. The feature #1 at the tip apex is enriched in Fe and significantly depleted in Ni and Mo (Table 3) and its crystallography could not have been identified, the measured composition do not agree with the composition of the residual delta ferrite because ferrite stabilizers as Cr and Mo, do not enrich within the feature #1 compared to the matrix. The feature #3, could not be associated with any defect of the tip imaged in STEM, the noise increase at its location indicates an APT artefact rather than a crystal defect.

As shown in Fig. 9, the feature #2 has the shape of a truncated dislocation loop. This loop is enriched in Ni and Si/N and depleted in Cr, Mn and Mo. Based on the dislocation loop morphology regarding crystallographic orientation, the loop lies on a {111} habit plane and can either be a faulted Frank loop or a perfect loop. This method used to identify dislocation loops in BCC alloys [40] by utilizing the anticipated dislocation morphologies developed by Yao et al. [41] have been extended to FCC alloys [10].

Table 3. Enrichment/depletion observed at features #1, #2 and #4 (core and shell) location compared to the matrix m. s.d = standard deviation. r.e. = relative error.

	Ni	Si/N	Cr	Fe	Mn	Mo	Nb	P	Enrichment	Depletion
$[X]_m$ in at.%	10,7	1,5	21,1	63,5	1,6	1,6	<0,1	<0,1		
s.d. in at.%	0,02	0,01	0,03	0,03	0,01	0,01	0,00	0,00		
r.e.	0,00	0,01	0,00	0,00	0,01	0,01	0,02	0,02		
$[X]_{\#1}$ in at.%	3,6	1,4	20,3	72,2	1,7	0,8	<0,1	<0,1		
s.d. in at.%	0,1	0,1	0,2	0,2	0,1	0,0	0,0	0,0		
r.e.	0,0	0,1	0,0	0,0	0,0	0,1	>0,2	>0,2		
$[X]_{\#1}/[X]_m$	0,3	0,9	1,0	1,1	1,1	0,5	1,0	1,0	Fe	Ni, Mo
$[X]_{\#2}$ in at.%	16,9	4,0	14,4	63,8	0,8	0,5	<0,1	<0,1		
s.d. in at.%	0,8	0,4	0,7	1,0	0,2	0,1	0,1	0,1		
r.e.	0,0	0,1	0,0	0,0	0,2	0,3	>0,6	>0,6		
$[X]_{\#2}/[X]_m$	1,6	2,6	0,7	1,0	0,5	0,3	1,0	1,0	Ni, Si/N	Cr, Mn, Mo
$[X]_{\#4\text{-core}}$ in at.%	33,7	16,0	10,7	16,6	1,8	4,5	6,5	10,1		
s.d. in at.%	1,0	0,8	0,7	0,8	0,3	0,4	0,5	0,6		
r.e.	0,0	0,0	0,1	0,0	0,2	0,1	>0,1	>0,1		
$[X]_{\#4\text{-core}}/[X]_m$	3,1	10,6	0,5	0,3	1,1	2,8	64,7	101,5	Ni, Si/N, Mo, Nb, P	Cr, Fe
$[X]_{\#4\text{-shell}}$ in at.%	38,2	6,7	8,1	45,7	0,6	0,7	<0,1	<0,1		
s.d. in at.%	1,0	0,5	0,6	1,1	0,2	0,2	0,0	0,0		
r.e.	0,0	0,1	0,1	0,0	0,3	0,3	>0,0	>0,0		
$[X]_{\#4\text{-shell}}/[X]_m$	3,6	4,5	0,4	0,7	0,4	0,4	1,0	1,0	Ni, Si/N	Cr, Fe, Mn, Mo

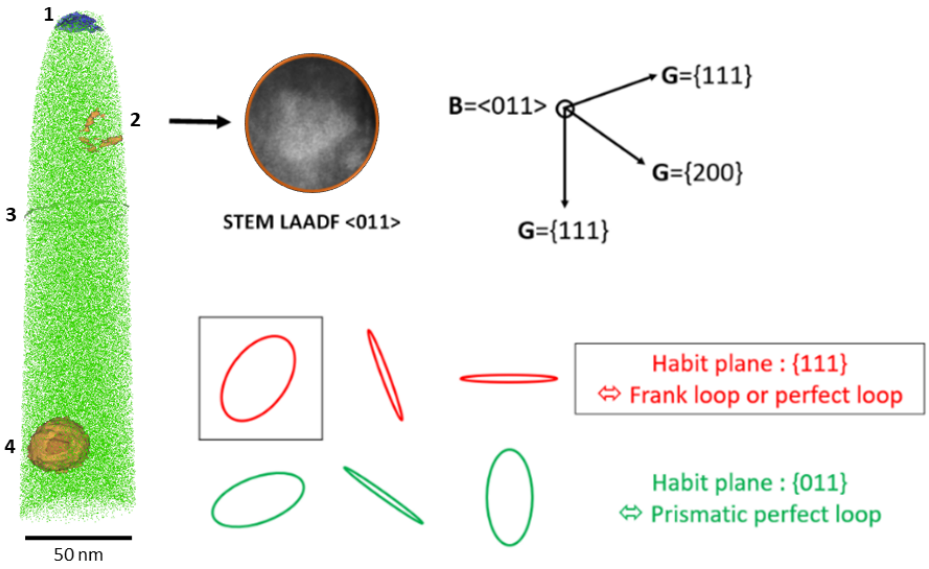

Fig. 9. (Color online) Observed features labelled within the APT volume. Close up view on the STEM LAADF image at **B**=<011> from Fig. 8c. Loop habit plane determination for faulted and perfect loops at **B**=<011> assuming that loops are circular.

A unique feature with a core-shell structure (Fig. 10 and 11) seems to be present within the APT volume at the feature #4 location. The core and the shell are less dense compared to the matrix, the ellipsoidal-shaped core exhibiting the lowest density (Fig. 11a). Relatively to the matrix, its shell is depleted in Fe, Cr, Mn and Mo and enriched in Ni and Si/N. Except N, these elements are known to be involved in RIS

and the observed trends are in line with the one observed in 316/L austenitic stainless steel grades [7], [11]. Contrary to Si, the presence of N is not confirmed as shown in Fig. 12.A.

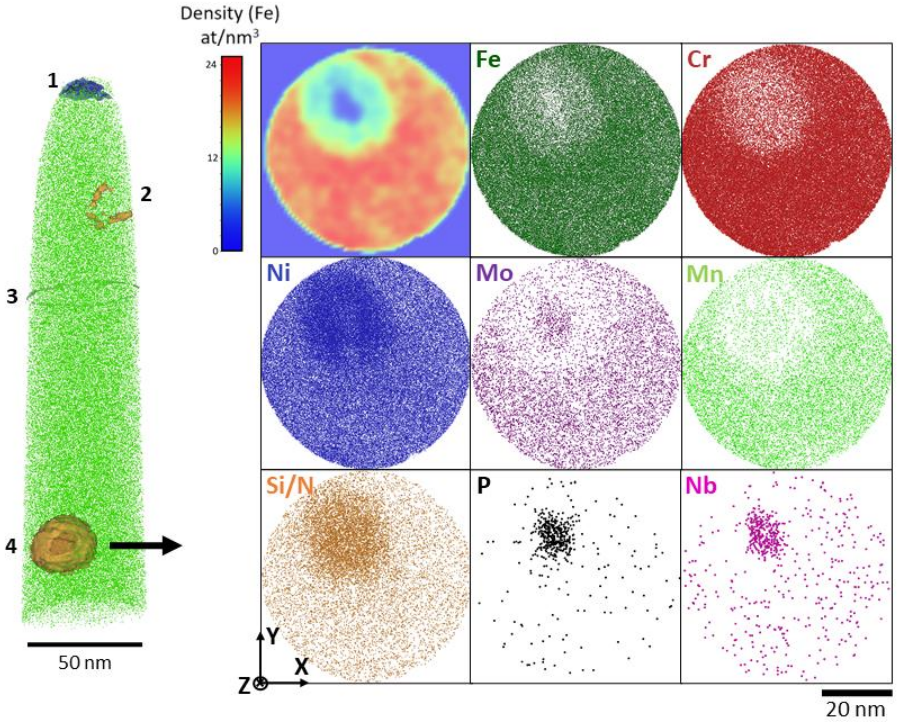

Fig. 10. (Color online) (X,Y) plane view of the feature #4 within the APT reconstructed volume, Fe density map and elemental distribution maps.

The core is depleted in Fe and Cr and enriched in Nb, P, Mo and Si/N. Since Ni^{2+}, Nb^{3+} and P^{+} contribute to the peak at 31 a.m.u., peak was decomposed twice: first time for Ni^{2+}+P^{+}, second time for Ni^{2+}+Nb^{3+}. The resulting two concentration profiles of Nb and P are displayed in Fig. 11b. Finally, relatively to the shell, core is enriched in Cr, Nb, P, Mo and Si/N. The highest Ni enrichment is observed at the core-shell interface. Ti has not been detected in the overall studied APT volume.

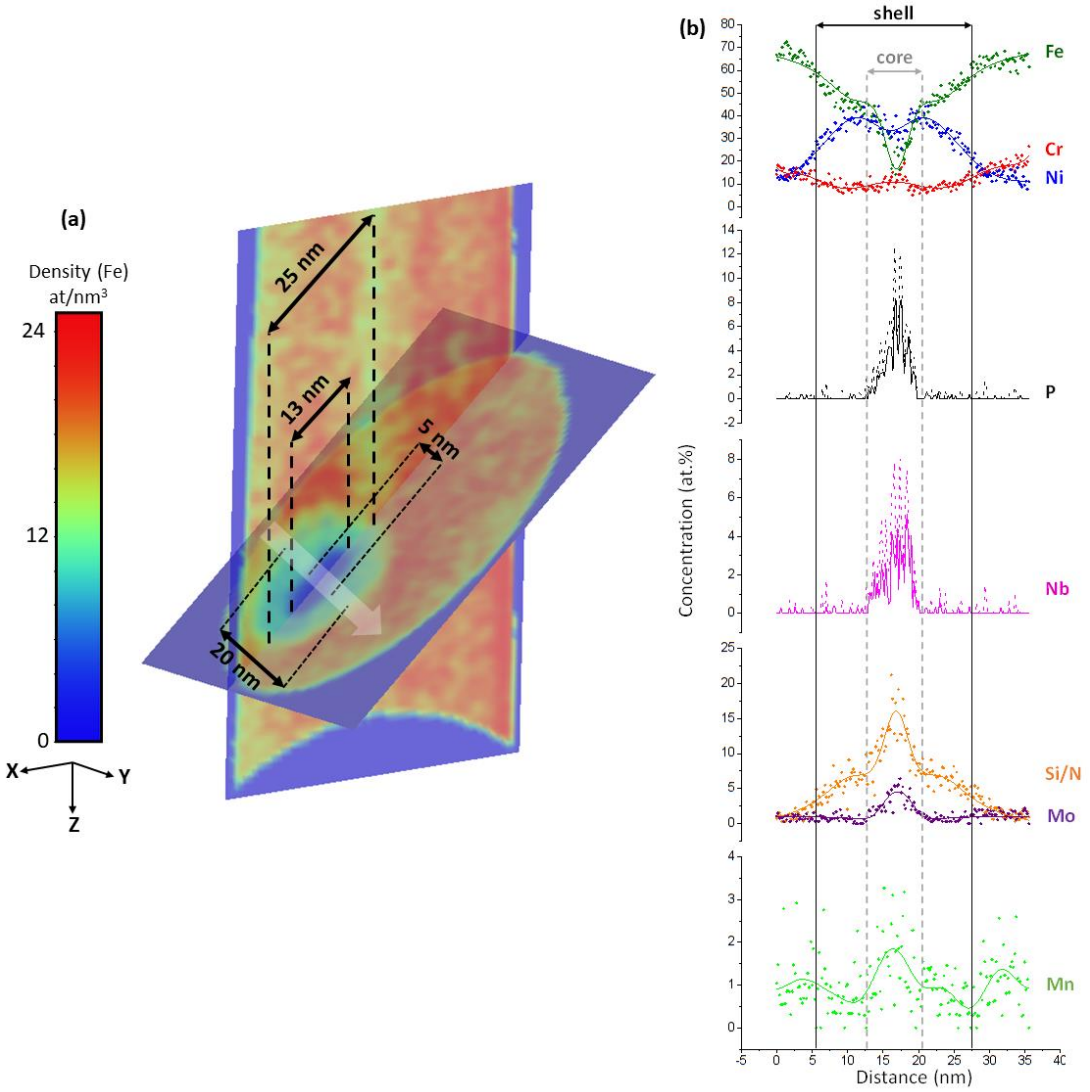

Fig. 11. (Color online) (a) Fe atoms density maps intersecting at the feature #4 location. (b) 1D concentration profiles passing through the feature with the z direction parallel to the smallest cluster core length (white transparent arrow in (a)).

$^{28}Si^{2+}$ and $^{14}N^{+}$ ions are superimposed in the M/n (mass over ionisation state ratio) peak at 14 a.m.u.. Because the two other isotopes of Si^{2+} at 14.5 and 15 a.m.u. are close to the background level, decomposition of the peak at 14 a.m.u. was not performed. Instead, abundances have been calculated from the total number of ions in the peak at 14 a.m.u. and the sum of Si^{2+} ions at 14.5 and 15 a.m.u.. The comparison of Si isotopes natural abundances with as calculated ones in Fig. 12a confirms the presence of Si both in the core and the shell of feature #4 whereas N seems to be absent. Indeed, at the core location, the number of detected counts in the peak at 14 a.m.u. is high enough to allow peak decomposition. As the natural abundance of nitrogen-14 is 99.6%, if N is present, then the calculated abundances along the profile would have been closer to 99.6% than 92.2%, the natural abundance of the main Si isotope at 14 a.m.u..

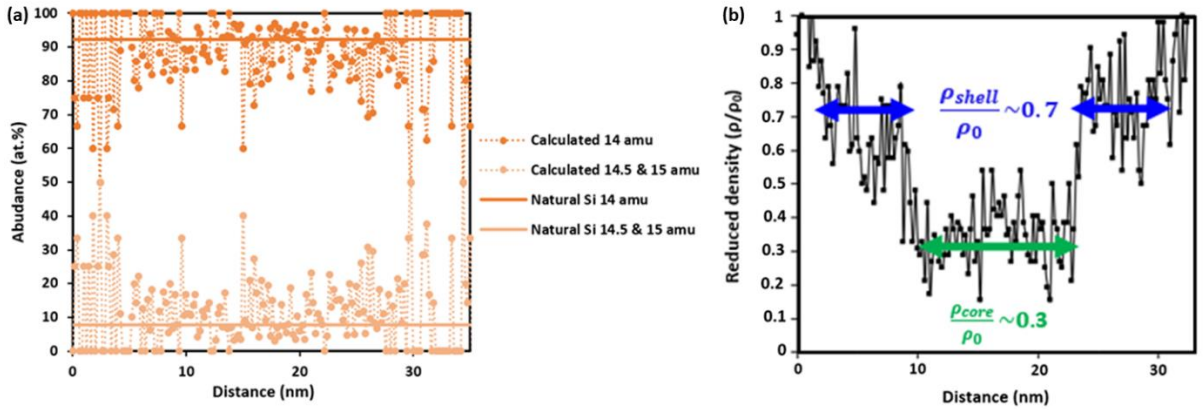

Fig. 12. (Color online) (a) Abundance linear profiles drawn to decorrelate Si and N relative contribution in their common peak at 14 a.m.u. and (b) reduced density profile passing through the feature with the z direction parallel to the smallest cluster core length (white arrow in Fig. 11.A).

Reduced density (measured atom density over calculated FCC Fe atom density) of the shell is equal to 0.7 while in the core it is equal to 0.3 (Fig. 12b). If the cluster core is a precipitate with an atomic density 3.3 times lower than the matrix (i.e. supposing that the evaporation field of the precipitate is the same as the matrix), then its atomic density is equal to 26 at.nm^{-3} resulting in a mass density of 2.1 $\pm$ 0.3 g.cm^{-3} (based on the chemical composition measured in the cluster core). This low mass density is far to suit with these following equilibrium phases or phases encountered in irradiated austenitic stainless steels: Fe_2P (6.9 g.cm^{-3}), FeP (6.2 g.cm^{-3}), gamma prime Ni_3Si (7.6 g.cm^{-3}), G phase $Mn_6Ni_{16}Si_7$ (7.0 g.cm^{-3}), Fe_2Mo (9.5 g.cm^{-3}), NbN (8.3 g.cm^{-3}) and Z-phase (7.7 g.cm^{-3}). It likely means that another feature could be included in this cluster. The feature #4 presented in Fig. 13 exhibits contrasts in STEM BF and LAADF modes that could be assigned to, at least, two different defects. One of them is spherical, it could possibly be a cavity, the other one is ellipsoidal, and is assumed to be a precipitate associated with the cavity. Presence of a cavity within the cluster could explain such a low value for reduced core density [44]. RIS on the cavity and the precipitate could correspond to the cluster shell while the precipitate having an evaporation field close to the matrix has an ellipsoidal shape, then may have not suffer from any distortion. These assumptions require to be confirmed by simulations.

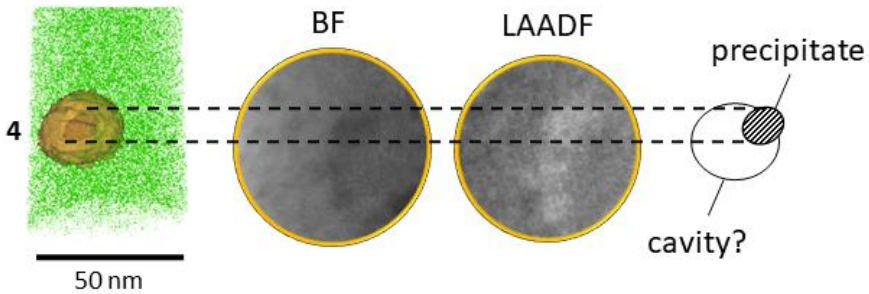

Fig. 13. (Color online) Close-up view of the feature #4 in the STEM LAADF image oriented at **B**=<011> (Fig. 8) and the scheme of suspected defects.

2. Discussion

After ion irradiation, cavities and Frank loops populations have been characterized at 1 dpa, 450°C. Obtained results are compared to the existing literature as presented in Fig. 14.

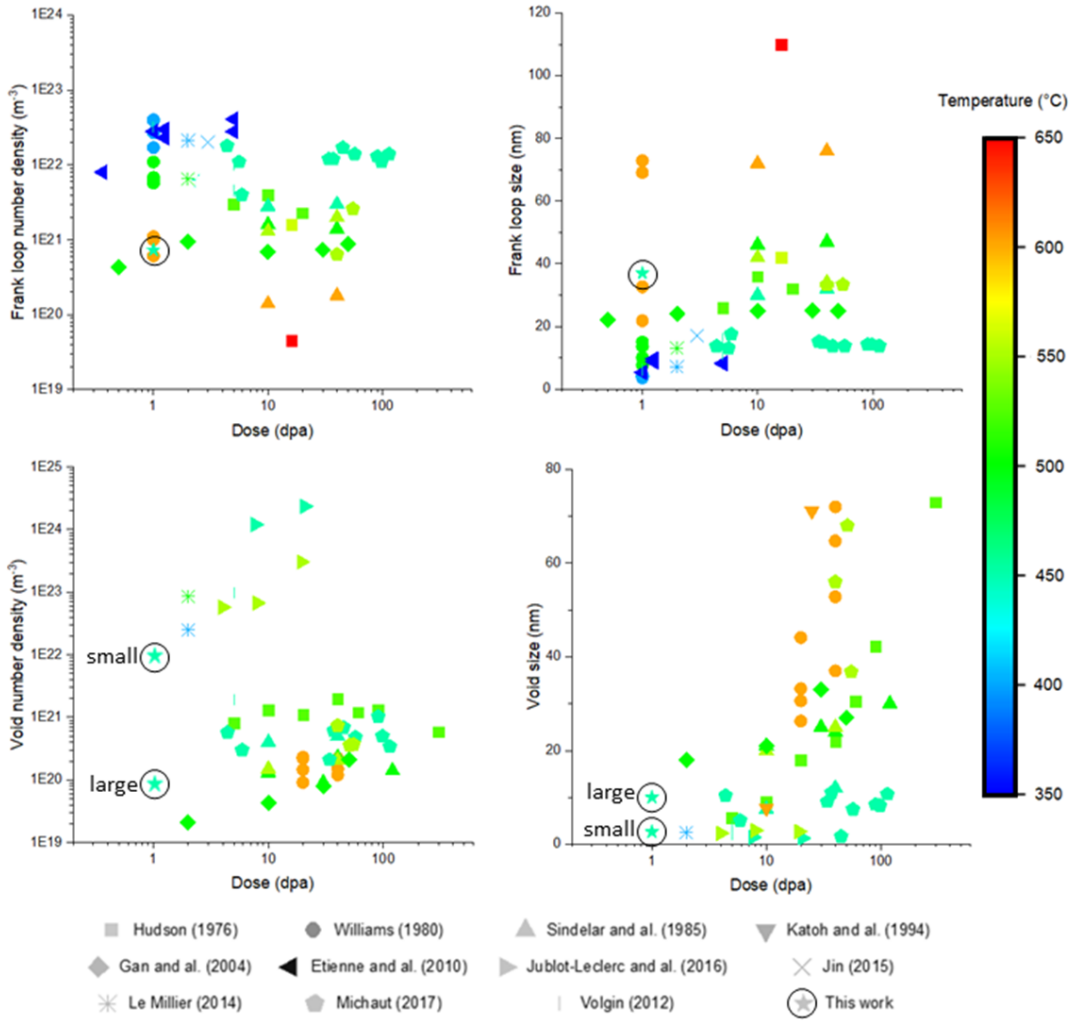

Fig. 14. (Color online) Microstructure evolution under irradiation in terms of Frank loops and cavities number density and size as a function of dose and temperature. Comparison of obtained results with the literature for various ion irradiated 304/L and 316/L austenitic stainless steels [11], [45]–[54] (non-exhaustive review).

Even if the dislocation density is higher than in common solution annealed austenitic stainless steel nuclear grades, the cavity number density and size of the two populations is in accordance with the reviewed literature. Nevertheless, it should be noted that irradiation to 1 dpa fits more with high temperatures for Frank loops. Ion beam heating depends on the thermal contact, heat could have been not well conducted and evacuated within the assembly. From this observation it is reasonable to suppose that the irradiation temperature was underestimated. Further experiments at irradiation conditions with well controlled temperature should be performed to study the measured discrepancy on microstructure evolution under irradiation.

After irradiation, common RIS trends are observed on dislocation loops and cavity/matrix interfaces (Fig. 15). RIS trends of major alloying elements can be explained by the Inverse Kirkendall Effect mechanism [55]. Cr, the fastest diffusing element deplete while slow diffusion of Ni provokes its enrichment at sinks. Fe depletion compensates Ni enrichment [56]. All the listed RIS mechanisms indeed compete. Fe exhibits a 'M-shaped' profile which could be explained by the competition between point defects concentration gradient and chemical potential gradient due to the segregation of elements at the vicinity of lattice defects. They are supposed to provoke an enrichment then a depletion respectively [57].

Self-interstitials (SIA) drag of undersized elements tends to enrich sinks as it is the case for Si and P [56]. Again, mechanisms compete and it has been shown from ab initio calculation [58] that Si can be affected by both SIA diffusion and vacancy drag. However, they show that the vacancy drag mechanism helps to enrich the Si at sinks under irradiation in austenitic systems.

P has been observed to segregate in 316/316L grades on almost all defect types: grain boundaries [7, 8, 11], dislocation loop and dislocation line [11]. Nevertheless, to our knowledge, P segregation on a cavity has only been reported in the case of void-precipitate association during neutron irradiation of austenitic stainless steels. Two types of phosphides Fe_2P and Fe_3P have been observed to be associated with cavities [59]. From the results of the current study, P was clearly segregating on cavities and was not observed to segregate on other defects neither from EDS nor APT analyses. Dislocations are known to be biased for SIA and P is generally thought to diffuse towards sinks via SIA-mediated mechanism [60]. Nevertheless, we observed experimentally P enrichments solely at cavities location, i.e. associated with precipitates, and not at dislocation loops. This fact suggests that precipitate-matrix interface probably exhibits a larger bias for SIA than dislocation loops. Moreover, SIA trapping by sinks could induce a local vacancy supersaturation at their vicinity responsible for cavities formation. Small cavities have been observed to trap a dislocation line whereas large cavities are observed being associated with precipitates. This second observation is in line with the proposed hypothesis which is: precipitate-matrix interface is more biased for SIAs than dislocations.

(a)

	ENRICHMENT								DEPLETION					
Defect type	Ni	Si	Mo	P	B	Cu	C	S	Fe	Cr	Mo	Mn	C	Cu
Grain boundary	2 3 6 7 10 11	2 3 6 7 10 11		2 3 7 10 11	7	2	7	7	2 3 6 7 10 11	2 3 6 7 10 11	2 3 6 11	2 7 10 11		7
Dislocation loop	7 8 11 12	7 8 11 12		7 8 11					7 8 11 12	7 8 11 12	11	7 8 11 12	11	7
Frank loop	9	9							9	9		9		
Dislocation line	4a 11	4a 11		11					11	11	11	11		
Cavity	3 9 12	3 9 12							3 9 12	3 9 12		9 12		
Ni-Si cluster			5	4a 4b 5										
Ni-Si-Mn cluster				1										

(b)

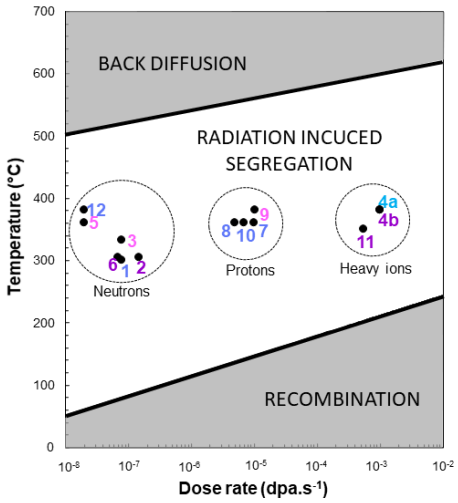

(c)

ASS grades	APT	STEM-EDS
304/304L	1 7 8 / 4a	10 12
316/316L	2 4b 11 / 5	6 / 3 9

Fig. 15. (Color online) (a) Elements enrichment and depletion at different sink-types depending on (c) the measurement technique in various austenitic stainless steels (1[61], [62] 2[7] 3[8] 4a,b[15] 5[63] 6[9] 7[10] 8[12] 9[14] 10[4] 11[11] 12[13]) and (b) the associated predicted RIS regime regarding the irradiation temperature and dose rate.

Nb enrichment at the location of a cavity is presumed to be caused by the existence of a precipitate or an embryo attached to the cavity. At the as-received state, Nb-rich Z-phase is the major precipitate observed but at this stage of investigation, a clear link between this Nb enrichment and the primary Z-phase could not be established. From the literature review, such enrichments at cavity location have never been reported yet neither in 314/L, 316/L and 316LN nor the Nb stabilized 347 and 348 grades. Z-phase stability under irradiation has not been studied yet in austenitic stainless steels.

Coupling S/TEM imaging with STEM-EDS allowed to associate different crystal defects to chemical redistribution under irradiation. However, two factors limit accurate quantification:

1/ Defects are surrounded by the matrix. The matrix contributes to the signal and the smaller the defect size to the lamella thickness ratio, the higher the matrix contribution.

2/ Several defects can be superimposed within the depth and their respective 3D morphology is not known. Hypotheses (e.g. defect shape, defect position within sample thickness) should be made to extract RIS levels on a defect, increasing measurements uncertainty.

APT gives access to a 3D representation of elemental distribution within the material. RIS levels could be quantitatively determined by this technique. Even if its high depth resolution allows to see atomic planes at poles location, lateral resolution is insufficient to identify precisely crystal defects, as it can be done with TEM. Nevertheless, if the tip orientation is known, it is sometimes possible to get information about defects crystallographic nature as it was the case for the dislocation loop labelled feature #2.

APT-TEM correlative microscopy takes benefit of both techniques to quantify RIS levels on intragranular defects.

The feature #4 core composition support the existence of a new phase after irradiation in the studied 316L(N) steel with similar enrichments as measured from STEM-EDS maps. Nevertheless, the feature #4 is not believed to be a precipitate, at least sole. The presence of a cavity associated with RIS at its interface with the matrix could explain such low value of reduced core density [44], but the shape of the reduced density profile does not match with the one obtained. However, from the observed contrasts in the close-up view of the cluster imaged by STEM, the presence of a precipitate associated with the cavity exhibiting RIS is suspected as it seems to be the case from S/TEM imaging associated with analytical STEM-EDS. Furthermore, apart from Fe, same enrichments are observed in both precipitate and the core of the feature #4. Such complex feature, i.e. cavity-precipitate association exhibiting RIS, in an APT reconstructed volume has not been reported yet and should induce field effects. Deeper investigations with associate simulations are needed to confirm this hypothesis.

Furthermore, the optimization of the TEM-APT correlative microscopy procedure is necessary. Indeed, as it is shown in Fig. 16, imaging a tip by TEM can make difficult contrast interpretation compared to images obtained from a lamella. Indeed, FIB damage remains at needle surface after the cleaning step (2kV) whereas a lower voltage ion cleaning with argon (0.5kV) in PIPS II is done on the case of TEM lamella. Also, the conical shape of the tip induces thickness variations along its diameter. An extra contrast due to thickness fringes in WBDF can be seen and HAADF images are more complex to interpret because contrast is not only due to Z but also to sample thickness.

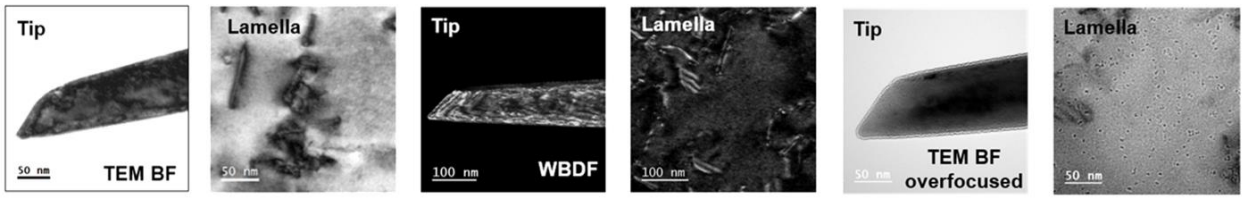

Fig. 16. (Color online) Comparison of contrast obtained from the tip analysed and a lamella for the same imaging conditions at the same scale for the 1 dpa 450°C irradiated state.

3. Conclusion

RIS on intragranular defects and phase stability under irradiation has been investigated in an optimized solution annealed 316L(N) austenitic stainless steel. The investigated steel has an increased content of N and a significant amount of Nb. At the as-received state, it exhibits a higher dislocation density than SA 316L nuclear grades and the primary Z-phase is dominant at the nanoscale. Coupled and correlated techniques were used to study 316L(N) chemical redistribution evolution after ion irradiation at 1 dpa 450°C on intragranular defects.

Dislocation loops were enriched in Ni and Si whereas cavities presented an additional enrichment in P. For the studied steel, precipitate-matrix interface is believed to be more biased for SIA than dislocations. Precipitate-cavity association is suspected, and the involved precipitate could be a Z-phase modified by irradiation.

S/TEM imaging associated with analytical STEM-EDS enabled to link defects crystallography to their chemistry but the high contribution of the surrounding matrix to the signal is a limitation for quantitative measurements. TEM-APT correlative microscopy was performed to overcome this issue. TEM-APT correlative microscopy allowed to determine the habit plane of a dislocation loop, to understand an APT artefact and it gave insights about the nature of a complex feature. This feature is suspected to be a Z-phase modified under irradiation associated with a cavity exhibiting Ni, Si and P enrichments induced by radiation. Nevertheless, to confirm the nature of this novel feature, further investigations of this steel at new irradiation conditions and simulations are needed.

CRediT authorship contribution statement

S. Rouland: Methodology, Investigation, Formal analysis, Visualization, Writing - Original Draft; Writing - Review & Editing. **B. Radiguet**: Conceptualization, Methodology, Supervision, Validation, Writing - Review & Editing. **P. Pareige**: Conceptualization, Methodology, Supervision, Validation, Writing - Review & Editing.

Declaration of competing interest

The authors declare that they have no known competing financial interests or personal relationships that could have appeared to influence the work reported in this paper.

Acknowledgements

To M. Blat-Yrieix and F. Delabrouille from EDF Lab Les Renardières for the material supply and fruitful discussions.

Experiments were performed on the GENESIS platform. GENESIS is supported by the Région Normandie, the Métropole Rouen Normandie, the CNRS via LABEX EMC3 and the French National Research Agency as a part of the program "Investissements d'avenir" with the reference ANR-11-EQPX-0020.

This research did not receive any specific grant from funding agencies in the public, commercial, or not-for-profit sectors.

Appendix A

The target temperature was 450°C but a large uncertainty on the irradiation temperature during irradiation experiment was observed. Indeed, almost 200°C difference was measured between the two installed thermocouples as shown in Fig. A.1. It seems to be likely due to a poor thermal contact between the two parts for the sample-holder. As no thermocouple was installed at the vicinity of irradiated samples surface, decision was made to model heat transfers by conduction and radiation in the sample-holder assembly (not convection because the specimen chamber was under vacuum) on COMSOL Multiphysics commercial software in order to estimate the temperature at samples level. A heating block was installed under the angled block. At its bottom surface the temperature was imposed to be the one measured by the thermocouple T_A. Thermal properties (i.e. thermal conductivity, thermal capacity and emissivity coefficient) were defined at 450°C for 316/L grades while mechanical properties were defined at room temperature. A parametric study was done in order to find the coupled parameters (i.e. rugosity and contact pressure) for which temperature at the washer level is equal to 391°C as measured by the thermocouple T_B. When T_A=593°C is imposed and the set rugosity and contact pressure result in T_B=391°C, the calculated temperature at samples level is equal to 450°C.

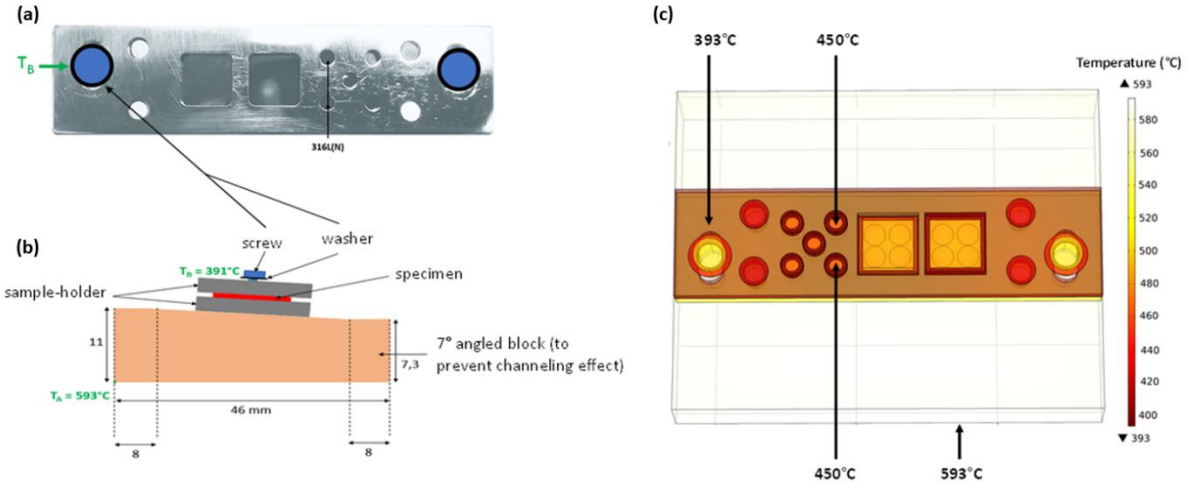

Fig A.1. (a) Specimen holder for irradiation, location of 316L(N) specimens and the closest thermocouple T_B from the irradiated specimen surface. (b) Scheme of the specimen holder assembly in the detector chamber and location of the thermocouples, note that all parts of the assembly (including specimens) are made from austenitic stainless steels. (c) Results from COMSOL heat transfer simulation.

Ion heating was ignored for the simulation, but it can be calculated separately thanks to the following expression [64]:

$$\Delta T = \frac{2J}{k_T}\left(\frac{k_T t}{\rho C_T}\right)^{\frac{1}{2}} \quad \text{(A-1)}$$

Where the thermal conductance k_T is equal to 0.209 $W.cm^{-1}.K^{-1}$ [65] and the specific heat C_T is equal to 1.52 W.s.g-1.K-1 [66] at 450°C, the density ρ was taken to be equal to 7.96 $g.cm^{-3}$ and t is the time in seconds. The beam power density J (in $W.cm^{-2}$) is given by :

$$J = \Phi \times E \times e \tag{A-2}$$

Here E is the beam energy in eV, e the elementary charge and Φ is the beam flux. To reach a fluence of $3.2x10^{15}$ $ions.cm^{-2}$ during a day session, $\Phi=1.2x10^{11}$ $ions.cm^{-2}.s^{-1}$. From this calculation, an increase in temperature of 20°C is expected. It was postulated that the temperature error is equal to this increase in temperature, therefore the irradiation temperature is estimated to be equal to 450 ± 20°C.

Appendix B

Supplementary Material.

References

[1] S. Şahin and M. Übeyli, 'A Review on the Potential Use of Austenitic Stainless Steels in Nuclear Fusion Reactors', *Journal of Fusion Energy*, vol. 27, no. 4, pp. 271–277, Dec. 2008, doi: 10.1007/s10894-008-9136-3.

[2] P. L. Andresen and G. S. Was, 'A historical perspective on understanding IASCC', *Journal of Nuclear Materials*, vol. 517, pp. 380–392, Apr. 2019, doi: 10.1016/j.jnucmat.2019.01.057.

[3] T. R. Allen, J. I. Cole, J. Gan, G. S. Was, R. Dropek, and E. A. Kenik, 'Swelling and radiation-induced segregation in austentic alloys', *Journal of Nuclear Materials*, vol. 342, no. 1–3, pp. 90–100, Jun. 2005, doi: 10.1016/j.jnucmat.2005.02.008.

[4] Busby, Was, and Kenik, 'Isolating the effect of radiation-induced segregation in irradiation-assisted stress corrosion cracking of austenitic stainless steels', *Journal of Nuclear Materials*, no. 302(1), pp. 20–40, 2002.

[5] Maziasz, 'Formation and stability of radiation-induced phases in neutron-irradiated austenitic and ferritic steels', *Journal of Nuclear Materials*, no. 169, pp. 95–115, 1989.

[6] Marwick, 'Segregation in irradiated alloys: the inverse Kirkendall effect and the effect of constitution on void swelling', *Journal of Physics F: Metal Physics*, no. 8(9), pp. 1849–1861, 1978.

[7] K. Fujii and K. Fukuya, 'Irradiation-induced microchemical changes in highly irradiated 316 stainless steel', *Journal of Nuclear Materials*, vol. 469, pp. 82–88, Feb. 2016, doi: 10.1016/j.jnucmat.2015.11.035.

[8] D. J. Edwards, E. P. Simonen, F. A. Garner, L. R. Greenwood, B. M. Oliver, and S. M. Bruemmer, 'Influence of irradiation temperature and dose gradients on the microstructural evolution in neutron-irradiated 316SS', *Journal of Nuclear Materials*, vol. 317, no. 1, pp. 32–45, Apr. 2003, doi: 10.1016/S0022-3115(03)00003-5.

[9] Fukuya, Fujii, Nishioka, and Kitsunai, 'Evolution of microstructure and microchemistry in cold-worked 316 stainless steels under PWR irradiation', *Journal of nuclear science and technology*, no. 43(2), pp. 159–173, 2006.

[10] Z. Jiao and G. S. Was, 'Novel features of radiation-induced segregation and radiation-induced precipitation in austenitic stainless steels', *Acta Materialia*, vol. 59, no. 3, pp. 1220–1238, Feb. 2011, doi: 10.1016/j.actamat.2010.10.055.

[11] A. Etienne, B. Radiguet, N. J. Cunningham, G. R. Odette, and P. Pareige, 'Atomic scale investigation of radiation-induced segregation in austenitic stainless steels', *Journal of Nuclear Materials*, vol. 406, no. 2, pp. 244–250, Nov. 2010, doi: 10.1016/j.jnucmat.2010.08.043.

[12] Y. Chen, P. H. Chou, and E. A. Marquis, ‘Quantitative atom probe tomography characterization of microstructures in a proton irradiated 304 stainless steel’, *Journal of Nuclear Materials*, vol. 451, no. 1–3, pp. 130–136, Aug. 2014, doi: 10.1016/j.jnucmat.2014.03.034.
[13] X. Liu, L. He, H. Yan, M. Bachhav, and J. F. Stubbins, ‘A transmission electron microscopy study of EBR-II neutron-irradiated austenitic stainless steel 304 and nickel-base alloy X-750’, *Journal of Nuclear Materials*, vol. 528, p. 151851, Jan. 2020, doi: 10.1016/j.jnucmat.2019.151851.
[14] M. Boisson, L. Legras, E. Andrieu, and L. Laffont, ‘Role of irradiation and irradiation defects on the oxidation first stages of a 316L austenitic stainless steel’, *Corrosion Science*, vol. 161, p. 108194, Dec. 2019, doi: 10.1016/j.corsci.2019.108194.
[15] Z. Jiao and G. S. Was, ‘Precipitate behavior in self-ion irradiated stainless steels at high doses’, *Journal of Nuclear Materials*, vol. 449, no. 1–3, pp. 200–206, Jun. 2014, doi: 10.1016/j.jnucmat.2014.02.026.
[16] M. Herbig, P. Choi, and D. Raabe, ‘Combining structural and chemical information at the nanometer scale by correlative transmission electron microscopy and atom probe tomography’, *Ultramicroscopy*, vol. 153, pp. 32–39, Jun. 2015, doi: 10.1016/j.ultramic.2015.02.003.
[17] C. M. Barr, P. J. Felfer, J. I. Cole, and M. L. Taheri, ‘Observation of oscillatory radiation induced segregation profiles at grain boundaries in neutron irradiated 316 stainless steel using atom probe tomography’, *Journal of Nuclear Materials*, vol. 504, pp. 181–190, Jun. 2018, doi: 10.1016/j.jnucmat.2018.01.053.
[18] A. Harte *et al.*, ‘Understanding irradiation-induced nanoprecipitation in zirconium alloys using parallel TEM and APT’, *Journal of Nuclear Materials*, vol. 510, pp. 460–471, Nov. 2018, doi: 10.1016/j.jnucmat.2018.08.033.
[19] B. Mazumder, C. M. Parish, and M. K. Miller, ‘Correlative TEM and APT of Helium Bubbles in Ion-Irradiated RAFM Steel’, *Microscopy and Microanalysis*, vol. 21, no. S3, pp. 587–588, Aug. 2015, doi: 10.1017/S1431927615003736.
[20] *RCC-MRx, Design. ‘Construction Rules for Mechanical Components of Nuclear Installations: high temperature, research and fusion reactors.’*, AFCEN. 2018.
[21] M. D. Mathew, K. Laha, and V. Ganesan, ‘Improving creep strength of 316L stainless steel by alloying with nitrogen’, *Materials Science and Engineering: A*, vol. 535, pp. 76–83, Feb. 2012, doi: 10.1016/j.msea.2011.12.044.
[22] J. Ganesh Kumar, M. Chowdary, V. Ganesan, R. K. Paretkar, K. Bhanu Sankara Rao, and M. D. Mathew, ‘High temperature design curves for high nitrogen grades of 316LN stainless steel’, *Nuclear Engineering and Design*, vol. 240, no. 6, pp. 1363–1370, Jun. 2010, doi: 10.1016/j.nucengdes.2010.02.038.
[23] Padilha and Rios, ‘Decomposition of austenite in austenitic stainless steels’, *ISIJ international*, no. 42.4, pp. 325–327, 2002.
[24] Sourmail, ‘Precipitation in creep resistant austenitic stainless steels’, *Materials science and technology*, no. 17(1), pp. 1–14, 2001.
[25] E. Cottereau, J. Camplan, J. Chaumont, R. Meunier, and H. Bernas, ‘ARAMIS: An ambidextrous 2 MV accelerator for IBA and MeV implantation’, *Nuclear Instruments and Methods in Physics Research Section B: Beam Interactions with Materials and Atoms*, vol. 45, no. 1–4, pp. 293–295, Jan. 1990, doi: 10.1016/0168-583X(90)90838-L.
[26] C.-O. Bacri *et al.*, ‘SCALP, a platform dedicated to material modifications and characterization under ion beam’, *Nuclear Instruments and Methods in Physics Research Section B: Beam Interactions with Materials and Atoms*, vol. 406, pp. 48–52, Sep. 2017, doi: 10.1016/j.nimb.2017.03.036.
[27] R. E. Stoller, M. B. Toloczko, G. S. Was, A. G. Certain, S. Dwaraknath, and F. A. Garner, ‘On the use of SRIM for computing radiation damage exposure’, *Nuclear Instruments and Methods in Physics Research Section B: Beam Interactions with Materials and Atoms*, vol. 310, pp. 75–80, Sep. 2013, doi: 10.1016/j.nimb.2013.05.008.
[28] L. Legras, M.-L. Lescoat, S. Jublot-Leclerc, and A. Gentils, ‘Optimisation of TEM preparation in metallic materials using low voltage ions’, presented at the European Microscopy Congress 2016 : Proceedings, 2016. doi: https://doi.org/10.1002/9783527808465.EMC2016.5973.
[29] R. F. Egerton, *Electron Energy-Loss Spectroscopy in the Electron Microscope*. Boston, MA: Springer US, 2011. doi: 10.1007/978-1-4419-9583-4.

[30] J. E. Bailey and P. B. Hirsch, 'The dislocation distribution, flow stress, and stored energy in cold-worked polycrystalline silver', *Philosophical Magazine*, vol. 5, no. 53, pp. 485–497, May 1960, doi: 10.1080/14786436008238300.
[31] C. J. Ulmer and A. T. Motta, 'Characterization of faulted dislocation loops and cavities in ion irradiated alloy 800H', *Journal of Nuclear Materials*, vol. 498, pp. 458–467, Jan. 2018, doi: 10.1016/j.jnucmat.2017.11.012.
[32] F. Danoix, G. Grancher, A. Bostel, and D. Blavette, 'Standard deviations of composition measurements in atom probe analyses—Part II: 3D atom probe', *Ultramicroscopy*, vol. 107, no. 9, pp. 739–743, Sep. 2007, doi: 10.1016/j.ultramic.2007.02.005.
[33] X. Yin *et al.*, 'Inclusion evolution during refining and continuous casting of 316L stainless steel', *Ironmaking & Steelmaking*, vol. 43, no. 7, pp. 533–540, Aug. 2016, doi: 10.1080/03019233.2015.1125599.
[34] C. Pokor, Y. Brechet, P. Dubuisson, J.-P. Massoud, and X. Averty, 'Irradiation damage in 304 and 316 stainless steels: experimental investigation and modeling. Part II: Irradiation induced hardening', *Journal of Nuclear Materials*, vol. 326, no. 1, pp. 30–37, Mar. 2004, doi: 10.1016/j.jnucmat.2003.12.008.
[35] R. E. Stoller, 'Modeling dislocation evolution in irradiated alloys', *MTA*, vol. 21, no. 7, pp. 1829–1837, Jul. 1990, doi: 10.1007/BF02647229.
[36] N. Hashimoto, E. Wakai, and J. P. Robertson, 'Relationship between hardening and damage structure in austenitic stainless steel 316LN irradiated at low temperature in the HFIR', *Journal of nuclear materials*, vol. 273, no. 1, pp. 95–101, 1999.
[37] V. Vodárek, 'Stability of Z-phase and M6X in creep-resistant steels', *Scripta Materialia*, vol. 66, no. 9, pp. 678–681, May 2012, doi: 10.1016/j.scriptamat.2012.01.024.
[38] Y. Li, Y. Liu, C. Liu, C. Li, and H. Li, 'Mechanism for the formation of Z-phase in 25Cr-20Ni-Nb-N austenitic stainless steel', *Materials Letters*, vol. 233, pp. 16–19, Dec. 2018, doi: 10.1016/j.matlet.2018.08.141.
[39] V. Vodárek, 'Creep behaviour and microstructural evolution in AISI 316LN+Nb steels at 650°C', *Materials Science and Engineering: A*, vol. 528, no. 12, pp. 4232–4238, May 2011, doi: 10.1016/j.msea.2011.02.025.
[40] C. M. Parish, K. G. Field, A. G. Certain, and J. P. Wharry, 'Application of STEM characterization for investigating radiation effects in BCC Fe-based alloys', *Journal of Materials Research*, vol. 30, no. 9, pp. 1275–1289, 2015.
[41] B. Yao, D. J. Edwards, and R. J. Kurtz, 'TEM characterization of dislocation loops in irradiated bcc Fe-based steels', *Journal of Nuclear Materials*, vol. 434, no. 1–3, pp. 402–410, Mar. 2013, doi: 10.1016/j.jnucmat.2012.12.002.
[42] Stubbins, Heuser, Hosemann, and Liu, 'Fundamental Studies of Irradiation-Induced Modifications in Microstructural Evolution and Mechanical Properties of Advanced Alloys', Univ. of Illinois at Urbana-Champaign, 14–6762, 2018.
[43] P. Xiu, H. Bei, Y. Zhang, L. Wang, and K. G. Field, 'STEM Characterization of Dislocation Loops in Irradiated FCC Alloys', *Journal of Nuclear Materials*, vol. 544, p. 152658, Feb. 2021, doi: 10.1016/j.jnucmat.2020.152658.
[44] X. Wang *et al.*, 'Interpreting nanovoids in atom probe tomography data for accurate local compositional measurements', *Nat Commun*, vol. 11, no. 1, p. 1022, Dec. 2020, doi: 10.1038/s41467-020-14832-w.
[45] Hudson, 'Void formation in solution-treated AISI 316 and 321 stainless steels under 46.5 MeV Ni6+ irradiation', *Journal of Nuclear Materials*, no. 60(1), pp. 89–106, 1976.
[46] Williams, 'The effect of soluble carbon on void swelling and low dose dislocation structures in type 316 austenitic stainless steel irradiated with 46.5 MeV Ni6+ ions', *Journal of Nuclear Materials*, no. 88(2–3), pp. 217–225, 1980.
[47] Sindelar, Kulcinski, and Dodd, 'Heterogeneous void formation in 14 MeV nickel-ion irradiated 316 SS', *Journal of nuclear materials*, no. 133, pp. 544–548, 1985.
[48] Katoh, Stoller, Kohno, and Kohyama, 'The influence of He/dpa ratio and displacement rate on microstructural evolution: a comparison of theory and experiment', *Journal of nuclear materials*, no. 210(3), pp. 290–302, 1994.

[49] J. Gan, E. P. Simonen, S. M. Bruemmer, L. Fournier, B. H. Sencer, and G. S. Was, 'The effect of oversized solute additions on the microstructure of 316SS irradiated with 5 MeV Ni++ ions or 3.2 MeV protons', *Journal of Nuclear Materials*, vol. 325, no. 2–3, pp. 94–106, Feb. 2004, doi: 10.1016/j.jnucmat.2003.11.002.
[50] S. Jublot-Leclerc, X. Li, L. Legras, M.-L. Lescoat, F. Fortuna, and A. Gentils, 'Microstructure of Au-ion irradiated 316L and FeNiCr austenitic stainless steels', *Journal of Nuclear Materials*, vol. 480, pp. 436–446, Nov. 2016, doi: 10.1016/j.jnucmat.2016.08.006.
[51] H.-H. Jin, E. Ko, S. Lim, and J. Kwon, 'Effects of helium and hydrogen on radiation-induced microstructural changes in austenitic stainless steel', *Nuclear Instruments and Methods in Physics Research Section B: Beam Interactions with Materials and Atoms*, vol. 359, pp. 69–74, Sep. 2015, doi: 10.1016/j.nimb.2015.07.086.
[52] Le Millier, 'Fragilisation des aciers inoxydables austénitiques sous irradiation: évolution de la microstructure et amorçage de la corrosion sous contrainte assistée par l'irradiation en milieu REP', Ecole Nationale Supérieure des Mines de Paris, 2014.
[53] B. Michaut, 'Caractérisation et modélisation de l'évolution de la microstructure et du gonflement d'aciers austénitiques représentatifs des internes inférieurs de Réacteur à Eau Pressurisée sous irradiations aux ions', Paris Saclay, 2017.
[54] A. Volgin, 'Characterization and understanding of ion irradiation effect on the microstructure of austenitic stainless steels', Université de Rouen, 2012.
[55] T. R. Allen and G. S. Was, 'Modeling radiation-induced segregation in austenitic Fe–Cr–Ni alloys', *Acta materialia*, vol. 46, no. 10, pp. 3679–3691, 1998.
[56] S. M. Bruemmer, E. P. Simonen, P. M. Scott, P. L. Andresen, G. S. Was, and J. L. Nelson, 'Radiation-induced material changes and susceptibility to intergranular failure of light-water-reactor core internals', *Journal of Nuclear Materials*, vol. 274, no. 3, pp. 299–314, 1999.
[57] D. Edwards, F. A. Garner, E. P. Simonen, and S. M. Bruemmer, 'Characterization of Neutron-Irradiated 300-Series Stainless Steels to Assess Mechanisms of Irradiation-Assisted Stress Corrosion Cracking: Volume 2: Core Components.', EPRI, 2001.
[58] L. Tan *et al.*, 'Microstructural Evolution of Type 304 and 316 Stainless Steels Under Neutron Irradiation at LWR Relevant Conditions', *JOM*, vol. 68, no. 2, pp. 517–529, Feb. 2016, doi: 10.1007/s11837-015-1753-5.
[59] Pedraza and Maziasz, 'Void-precipitate association during neutron irradiation of austenitic stainless steel', Oak Ridge National Laboratory, CONF-860605-33, 1987.
[60] H. Watanabe, A. Aoki, H. Murakami, T. Muroga, and N. Yoshida, 'Effects of phosphorus on defect behavior, solute segregation and void swelling in electron irradiated Fe-Cr-Ni alloys', *Journal of Nuclear Materials*, vol. 155–157, pp. 815–822, Jul. 1988, doi: 10.1016/0022-3115(88)90422-9.
[61] T. Toyama *et al.*, 'Irradiation-induced precipitates in a neutron irradiated 304 stainless steel studied by three-dimensional atom probe', *Journal of Nuclear Materials*, vol. 418, no. 1–3, pp. 62–68, Nov. 2011, doi: 10.1016/j.jnucmat.2011.07.027.
[62] W. Van Renterghem, A. Al Mazouzi, and S. Van Dyck, 'Influence of post irradiation annealing on the mechanical properties and defect structure of AISI 304 steel', *Journal of Nuclear Materials*, vol. 413, no. 2, pp. 95–102, Jun. 2011, doi: 10.1016/j.jnucmat.2011.04.006.
[63] B. Radiguet, A. Etienne, P. Pareige, X. Sauvage, and R. Valiev, 'Irradiation behavior of nanostructured 316 austenitic stainless steel', *Journal of Materials Science*, vol. 43, no. 23–24, pp. 7338–7343, Dec. 2008, doi: 10.1007/s10853-008-2875-8.
[64] E. G. Fu, A. Misra, H. Wang, L. Shao, and X. Zhang, 'Interface enabled defects reduction in helium ion irradiated Cu/V nanolayers', *Journal of Nuclear Materials*, vol. 407, no. 3, pp. 178–188, Dec. 2010, doi: 10.1016/j.jnucmat.2010.10.011.
[65] C. L. Hogan and R. B. Sawyer, 'The Thermal Conductivity of Metals at High Temperature', *Journal of Applied Physics*, vol. 23, no. 2, pp. 177–180, Feb. 1952, doi: 10.1063/1.1702169.
[66] R. F. Redmond and J. Lones, 'Enthalpies and heat capacities of stainless steel (316). zirconium. and lithium at elevated temperatures', Oak Ridge National Lab., 1342, 1952.

Supplementary Material for

Investigating radiation-induced segregation on intragranular defects in a 316L(N)

Solène Rouland, Bertrand Radiguet, Philippe Pareige

Normandie Université, UNIROUEN, INSA Rouen, CNRS, Groupe de Physique des Matériaux, 76000 Rouen, France.

Corresponding author: solene.rouland@univ-rouen.fr

Scanning electron microscopy (SEM) coupled with electron back-scattered diffraction (EBSD) and energy dispersive X-Ray spectroscopy (EDS) was performed on the as-received material to study microstructure heterogeneities at the micron-scale. Measurements were done on the Dual-Beam SEM-FIB (Focused Ga Ion Beam) microscope Zeiss XB-540. On the acquired maps, RD_1 and RD_2 refer to the rolling directions whereas ND denotes the normal direction. RD_1 is the direction of the last cross rolling pass thus RD_2 can also be noted as the transverse direction.

A simultaneous EBSD-EDS map has been collected by TEAM software on the same area of the specimen. EBSD data (Fig. S1a to d) were post-treated with OIM analysis software. A phase map was extracted allowing to calculate the surface fraction of austenite over the residual delta-ferrite which is higher than 0.99. The initial microstructure exhibits equiaxed grains of austenite of approximately 50 µm size with no pronounced preferential crystallographic orientation. More than half of the boundaries are twin boundaries. Delta-ferrite is elongated along the rolling direction RD_1. Ferrite is shaped as strips in both rolling directions (RD_1 and RD_2) which suggests that it has a ribbon shape (EDF R&D private communication).

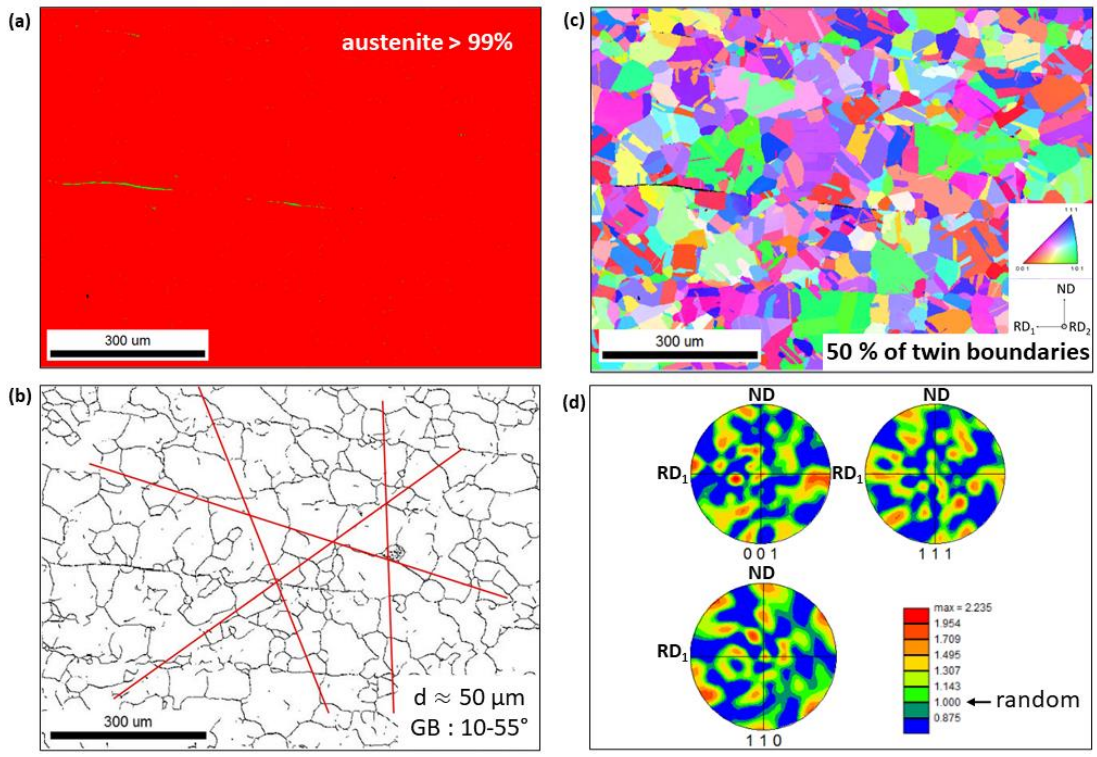

Fig. S1. SEM-EBSD (a) Phase map (red: austenite, green: delta ferrite), (b) random high-angle grain boundary map (excluding coincident site lattice boundaries and low-angle boundaries) with red lines drawn for grain size measurement by the intercept method, (c) orientation map (i.e. inverse pole figure map) and (d) pole figures along low-index directions: [001], [111] and [110].

In Fig. S2, SEM-EDS elemental maps reveal alpha-stabilizers (i.e. Cr, Mo, Si) enrichments not only at the ferrite location but at lower levels within the austenitic matrix as well. These chemical heterogeneities are referred as microsegregations, they are also enriched in Mn, an element known as a gamma-stabilizer. These microsegregations are parallel to the rolling directions and spaced of about 50 µm from each other.

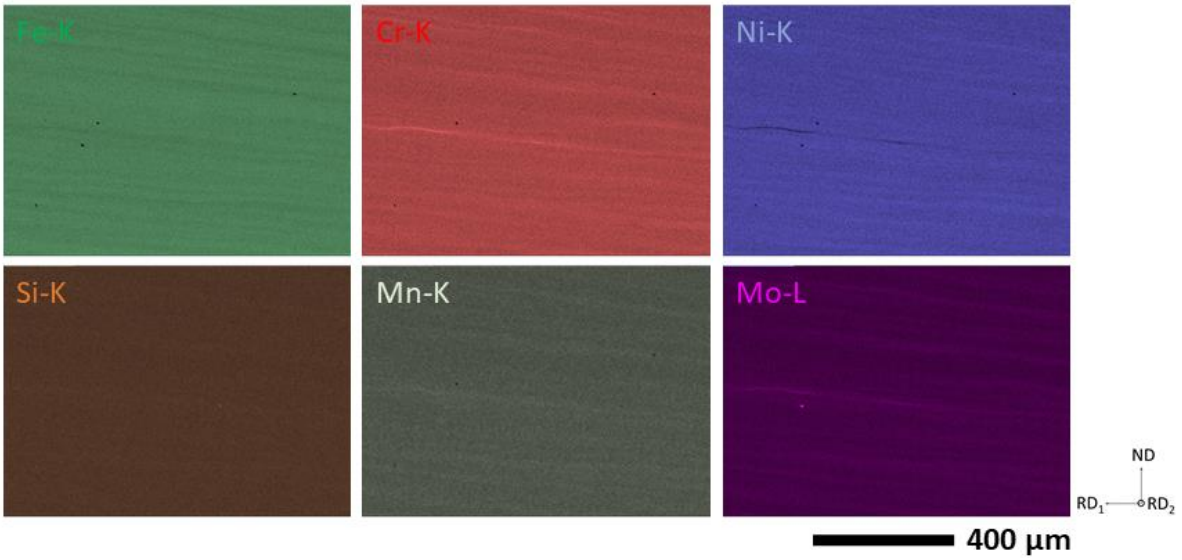

Fig. S2. SEM-EDS elemental maps.

Coupled EBSD-EDS acquisition also permitted to highlight the presence of micron-sized second phases (i.e. inclusions and precipitates) within the scanned area (Fig. S3a). Most of the identified particles are aluminium oxides, one of them being enriched in yttrium. Silicon oxide particles, also observed, could be either an inclusion or coming from the last step of polishing with OP-S during specimen preparation. Nb-rich precipitates are observed as well. An EDS spectrum (Fig. S3b) extracted from one of them shows that this Nb-precipitate is also enriched in N and Cr. Other EDS spectra indicate that Nb-rich precipitates are sometimes enriched in Ti or Mo. At the electron accelerating voltage of 20kV, K rays of Nb and Mo are not detected. L rays of Nb and Mo overlap, but, looking attentively to the corresponding peak shape and the relative intensity of their respective theorical rays, it is possible to unambiguously determine the presence/absence of these elements from spectrum analysis.

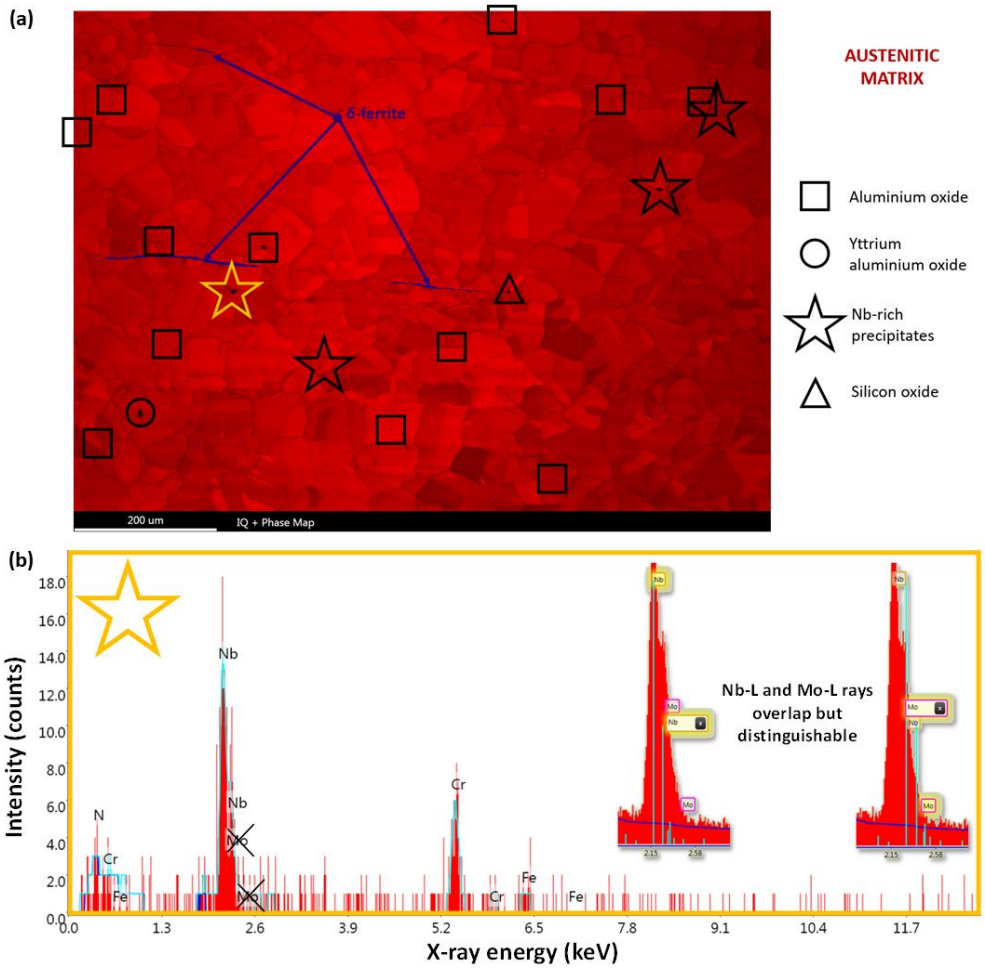

Fig S3. (a) Superimposed index quality map and phase map from EBDS data showing distribution of inclusions and second phases within the austenitic matrix. (b) SEM-EDS spectrum of the yellow star labelled precipitate, enriched in N, Nb and Cr. Indexation of the peak at 2.15 keV, discrimination between Nb-L and Mo-L rays.